Evaluating Primary Marine Aerosol Production and Atmospheric Roll Structures in Hawaii's Natural Oceanic Wind Tunnel*

VLADIMIR N. KAPUSTIN, ANTONY D. CLARKE, STEVEN G. HOWELL, CAMERON S. MCNAUGHTON, VERA L. BREKHOVSKIKH, AND JINGCHUAN ZHOU+

School of Ocean and Earth Science and Technology, University of Hawaii at Manoa, Honolulu, Hawaii

(Manuscript received 4 May 2011, in final form 25 January 2012)

ABSTRACT

Topography-induced steady-state accelerated wind flow in the Alenuihaha Channel between the islands of Hawaii and Maui provides about 100 km of fetch with winds that can nearly double over trade wind speed. Here ship- and aircraft-based observations of meteorological parameters and aerosols in Hawaii's orographic natural "wind tunnel" are used for the study of sea salt aerosol (SSA) production, evolution, and related optical effects under clean oceanic conditions. There are certain advantages of channel measurements, such as a broad and uniform upstream area usually filled with background aerosol, stationary flow, and known fetch, but also some difficulties, like vigorous entrainment and persistent presence of organized structures (rolls). It is found that marine boundary layer (MBL) rolls are a common occurrence near the Hawaiian Islands even when cloud streets are not visible in satellite imagery. The presence of rolls tends to enhance the variability of ambient aerosol concentration and probably affects production of primary sea salt aerosol and entrainment from above. The possibility of channel measurements of the size-dependent flux of SSA is explored using a concentration buildup method as surface wind speeds range from 7 to 11 m s^{-1}. Production of SSA particles with dry diameter as small as 0.18 μm was observed. General agreement with reported SSA fluxes was found.

1. Introduction

In the remote marine atmosphere there are four principal sources of natural aerosols. Sea salt aerosol (SSA) production by wind and breaking waves is the dominant source of primary aerosol mass (Lewis and Schwartz 2004). In situ atmospheric oxidation of reduced sulfur derived from marine dimethyl sulfide (DMS) emission is another source of marine boundary layer (MBL) aerosol (Clarke et al. 1998b; Kulmala et al. 2004). Entrainment of aerosol from the free troposphere in many cases is expected to dominate MBL aerosol number concentrations (Clarke et al. 1998a). The final source of aerosol number/mass in the MBL is the advection of natural continental aerosol into the MBL. This process is important in the coastal environment but is less important over the remote ocean because of the short atmospheric residence times of these aerosols (Raes et al. 2000).

The evolution of atmospheric aerosol in the MBL is controlled by gas and particle interactions (e.g., trace gas and particle fluxes, condensation, coagulation, and heterogeneous chemistry), as well as cloud processing, precipitation scavenging, and dry deposition. These microphysical processes are functions of thermodynamic (temperature and relative humidity) and dynamic (synoptic weather, local wind speed, and turbulence) processes that control atmosphere–ocean interactions and MBL structure at larger spatial and/or temporal scales.

Collectively, these processes control the number of aerosol acting as cloud condensation nuclei (CCN) in a dynamic system of aerosol–cloud feedbacks that affect the optical and microphysical characteristics of clouds, cloud lifetimes, and their precipitation patterns. To predict the direct and indirect effects of anthropogenic emissions of aerosol and their precursors on Earth's radiation balance requires a much better, more complete understanding of these aerosol–cloud interactions (Solomon et al. 2007).

There is ample evidence to suggest that SSA plays an important role in radiative transfer, cloud formation and properties, and chemistry and optics of the marine

* School of Ocean and Earth Science and Technology Contribution Number 8570.

+ Current affiliation: Alstom Power Group AB, Sweden.

Corresponding author address: Vladimir Kapustin, University of Hawaii, 1000 Pope Rd., MSB 531, Honolulu, HI 96822.
E-mail: kapustin@soest.hawaii.edu

DOI: 10.1175/JTECH-D-11-00079.1

atmosphere. To correctly assess the role of SSA, accurate estimates of the size-resolved sea-spray source function (SSSF) are required (de Leeuw et al. 2011). The number production flux of marine aerosols is dominated by sizes less than 0.3 μm, as determined from atmospheric measurements over the open ocean, the surf zone, and from aerosols produced artificially. Historically, SSSF measurements relied upon indirect methods and assumptions that are difficult to verify, and only recently have direct flux estimates become available (Nilsson et al. 2001). Chemically resolved fluxes present even greater challenges. As a result, significant differences by up to a factor of 5 exist between SSSF from different studies (de Leeuw et al. 2011; Lewis and Schwartz 2004; O'Dowd and De Leeuw 2007).

Methods that can be used to determine SSSF were discussed in details by Lewis and Schwartz (2004) and de Leeuw et al. (2011) and include field measurement and laboratory-based methods. Among the methods based on ambient aerosol measurement, the concentration buildup method (CBM) can be viewed as one of the few direct measurements of the upward flux in the real environment (Reid et al. 2001). The method calculates SSSF from the increase in vertical integral (column burden) of SSA as a function of downwind distance. Because the CBM is based on sufficiently dense spatial measurements quasi-stationary conditions are important. The non-steady-state condition for which SSA production is not balanced by removal is also an important consideration. However, losses resulting from dry deposition are generally minor corrections for measurement regions far from steady state, at least for particles sizes below about 10 μm. CBM directly relates changes in column burden to SSSF and is free from many assumptions of other methods (Hoppel et al. 2002; Lewis and Schwartz 2004). To date CBM has been implemented only once by Reid et al. (2001) for aircraft measurements of the buildup of SSA in the offshore advection of the east coast of the United States (Duck, North Carolina). Among the main concerns with CBM are the applicability of the aerosol production in the nearshore region to open-ocean conditions and relatively low concentration of SSA in smaller size ranges compared to the background continental aerosol.

The trade wind cumulus-topped MBL represents one of the largest meteorological regimes over the global ocean and encompasses the islands of Hawaii. A multilayer structure usually exists with a turbulent surface mixed layer (SML) overlaid by a second layer characterized by intermittent turbulence often related to clouds. Because this second layer serves as a mixing zone for SML and air from the free troposphere (FT), it is usually called a buffer layer (BuL).

Mesoscale shallow convection, and in particular large-scale horizontal structures (rolls) in the form of persistent organized counterrotating vortices, is a common feature of the MBL and is believed to contribute significantly to the bidirectional transport of aerosol, heat, and moisture (Brooks and Rogers 1997; Brummer 1999; Brummer et al. 1985; LeMone 1973, 1976; Weckwerth et al. 1997; Young et al. 2002). Major axes of rolls are aligned with the mean MBL wind shear vector. The wavelength of rolls, measured from updraft to updraft in the cross-roll direction, is about 3 times the depth of the rolls. A review of the environmental conditions that favor rolls suggests that roll structures can form under a variety of conditions (Atkinson and Zhang 1996; Brummer 1999; Brummer et al. 1985; Weckwerth et al. 1997; Young et al. 2002). However, most studies indicate that rolls are frequently present in near-neutral to moderately unstable conditions if there is a sufficient (usually vertical) wind shear. The existence of rolls can significantly change the fluxes within the boundary layer and at the surface. When favorable thermodynamic conditions are present, cloud streets form in the updraft regions between the rolls. Studies using lidar highlight the complexity of the aerosol and relative humidity fields when rolls are present (Dupont et al. 1994; Engelmann et al. 2008; Kiemle et al. 1995; Melfi et al. 1985). Recent modeling of the roll convection using a large eddy simulation (LES; Huang et al. 2009) and the comparison to aircraft observation indicates that stronger moist updrafts existed in the nonroll convection, whereas roll convection gave a more symmetrical distribution of up- and downdrafts, with stronger downdrafts than the nonroll case.

Organized structures (rolls) can and probably will complicate SSA measurements and SSSF estimates because of the following several reasons: 1) Resulting from the large updraft regions sea salt (or perhaps just the largest particles) can propagate farther up than would otherwise be the case (Marsham et al. 2008). As a result some CCN effects on clouds or precipitation are possible. 2) The presence of rolls can change entrainment rates, diluting sea salt either more or less than would otherwise happen, bringing FT material down, lowering RH, and suppressing hygroscopic growth, increasing visibility (Bigg et al. 1996, 2001). 3) Rolls affect the turbulence field (Kalogiros and Wang 2011), and can distort flux calculations because the long period does not work with eddy correlation time scales (Brooks and Rogers 1997).

Trade winds around Hawaii

Our studies of sea salt aerosol (SSA) near Hawaii include characterization of SSA size distributions, optical properties, and SSSF (Clarke et al. 2006; Clarke

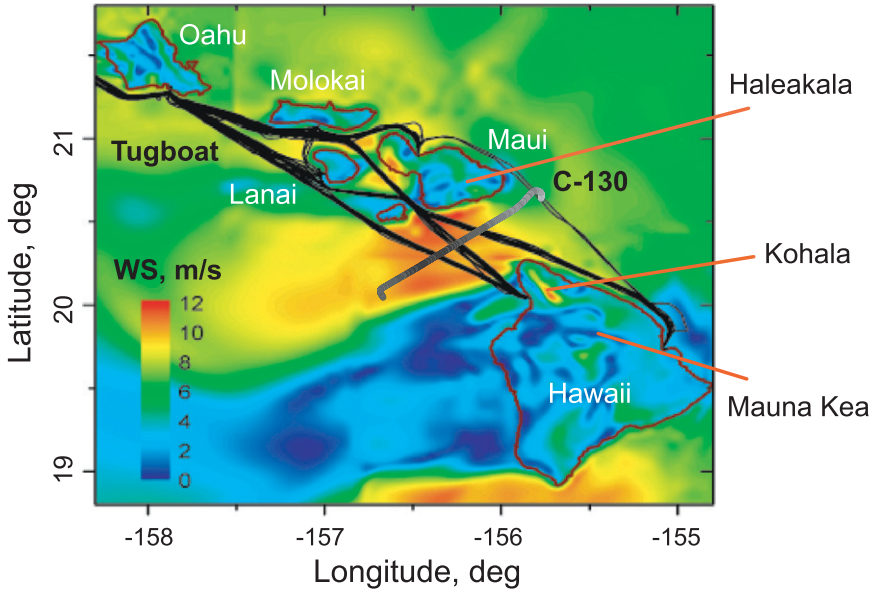

FIG. 1. MM5 simulations show a near doubling of wind speeds in the Alenuihaha Channel. Also shown are interisland tug boat routes (black), flight track at altitude 220 m for the 7 Aug 2007 PASE C-130 flight (gray), island names (white), and major mountain peaks (indicated by red lines).

and Kapustin 2002; Kapustin et al. 2006; Shinozuka et al. 2004). We found that the "natural wind tunnels" (Fig. 1) formed between Hawaiian Islands represent a suitable environment for CBM experiments. A typical "mountain gap flow" (Gabersek and Durran 2004) is created when the prevailing northeast trade winds are confined between the mountains of Maui (Haleakala at 3055 m) and Hawaii (Kohala at 1700 m and Mauna Kea at 4207 m), that rise near to or above the TWI. The unique features of this region are a broad and fairly uniform upstream area with steady-state trade wind flow sustaining a background marine aerosol. Channeled flow between the islands often leads to predictable stationary-enhanced wind flow aligned along the 100-km fetch of the Alenuihaha Channel (AC) and others that generate enhanced whitecaps and SSA and persistent cloud patterns (rolls) within the enhanced wind area of the channel.

The fifth-generation Pennsylvania State University (PSU)–National Center for Atmospheric Research (NCAR) Mesoscale Model (MM5) simulations for the Hawaiian Islands (Fig. 1) provided by the University of Hawaii's Department of Meteorology and direct aerial observation (Smith and Grubisic 1993; Yang and Chen 2008; Yang et al. 2008) show that wind speed in the Alenuihaha Channel can nearly double along a fetch of more than 100 km (the red/yellow area on Fig. 1). A doubling of wind speed nearly triples the wind stress, enhancing sea salt production by wind and breaking waves.

Mountain gap flow simulations (Gabersek and Durran 2004; Zangl 2002) identified three gap-flow regimes based on the nondimensional mountain height $h = 1/\mathrm{Fr}$, where Fr is the Froude number ($\mathrm{Fr} = U/Nbv{*}H$, where U is the upstream wind speed, Nbv is the Brunt–Väisälä frequency, and H is the maximum mountain height). In the linear regime ($h \ll 1$) simulations show a slight enhancement of the wind within and downstream of the gap, but there is no distinct jet of high winds emanating from the gap. For very high mountains ($h \gg 2$, upstream-blocking regime) the lee vortex patterns exist behind the mountain, but the jet winds emanating from the gap in the exit region are weaker than the undisturbed upstream flow. For an intermediate height range ($h \sim 1.5$, the mountain wave regime) the flow accelerates through the gap and upper part of the mountain slope, the gap jet extends far downstream, and the highest winds occur along the gap. A narrow zone of high winds ends abruptly in a feature analogous to a hydraulic jump. A turbulent wake of decelerated flow is present downstream of the jump (Gabersek and Durran 2004; Zangl 2002). For Kohala, a typical upstream wind of $U = 10\ \mathrm{m\ s^{-1}}$ and $N = 0.01\ \mathrm{s^{-1}}$ yields $h = 1.7$, which corresponds to the mountain wave regime when a hydraulic jump is present. Locations of hydraulic jumps within the Alenuihaha can be identified using the Moderate Resolution Imaging Spectroradiometer (MODIS) satellite images. Figure 2 reveals that cloud streets (rolls) are present within the channel. Rolls are a common feature of the AC and

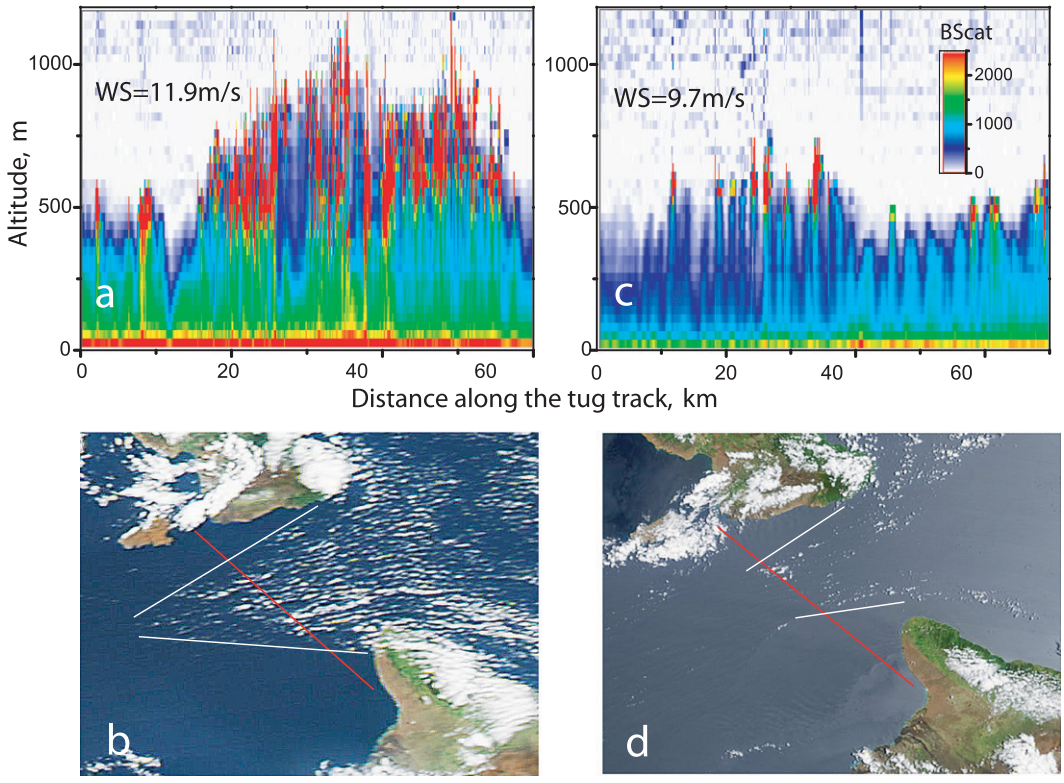

FIG. 2. Ceilometer backscatter profiles (10^{-9} m^{-1} srad^{-1}) during crossing of the Alenuihaha Channel between Maui and the Big Island of Hawaii. (a),(c) Clouds are evident as high backscatter values in the ceilometer data with the columns of high backscatter (red) below clouds, and the lower backscatter (blue) in the adjacent cloud-free regions. (b),(d) Tugboat routes (red) superimposed upon MODIS images revealing related cloud streets for the same days.

were detected at wind speeds ranging from 5 to 12 m s^{-1}. The resulting cloud streets (Fig. 2b) exist mostly within the wedge pattern. Edges of the cloud street triangle (white line on the figure) coincide with expected locations of hydraulic jumps (Smith and Grubisic 1993). A similar wedge pattern exists also with much weaker cloudiness (Fig. 2d). The exact location and shape of the hydraulic jump wedge pattern depends on trade wind speed and direction.

Here we examine boundary layer structure and aerosol properties within the Alenuihaha Channel and assess the potential of this ''natural wind tunnel'' for making SSSF measurements using CBM. The influence of large organized structures on sea spray aerosol parameters is also examined.

2. Observational platforms and measurements

Measurements of MBL structure and aerosol properties were conducted aboard a commercial tugboat (Young Brothers, Ltd.) traveling between Oahu, Maui, and Hawaii every few days in March–August 2005. In situ aerosol measurements included total (TotScat), submicrometer (SubScat), and supermicrometer (SupScat = TotScat − SubScat) light scattering measured by the Radiance Research M903 nephelometer (wavelength 530 nm) with an inlet impactor (aerodynamic size cut at 1 μm) to periodically remove the larger aerosol and resolve contributions to scattering from particles above and below this size; total and refractory (T = 360°C) aerosol number concentrations of particles with dry diameters $D_p > 10$ nm [TSI model 3010 condensation nuclei (CN) counter with $\Delta T = 22°$]; number concentrations of particles with dry aerodynamic particle diameters D_{aer} = 0.8–10.0 μm (TSI model 3321 APS); and ambient droplet diameters D_{amb} = 2–20.0 μm (DMT model CDP). Measured environmental parameters included temperature T, relative humidity RH, wind speed WS, and wind direction WD. Boundary layer structure was detected with Vaisala ceilometer model CT25K, which was operative using their high-sensitivity algorithm. The CT25K is a single-lens lidar system with a pulsed near-infrared diode laser (wavelength 905 nm), which is most sensitive to rain and cloud droplets but able to detect coarse aerosol particles. The ceilometer retrieval algorithm allowed us to qualitatively map clouds,

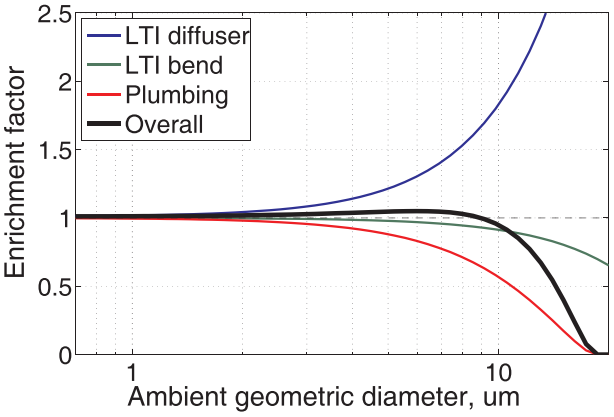

FIG. 3. LTI particles enhancement factor (blue), particles losses in the bend behind LTI (green), plumbing tubing losses (red) and overall LTI enrichment factor (black) for APS aerosol measurements. Particles in the LTI and the bend were assumed to be at the size and density given by the ambient RH (77%), while losses in the tubing were calculated at the 48% RH of the APS inlet.

precipitation, and SML aerosol vertical structure with 30-m resolution (Clarke and Kapustin 2003).

In situ airborne measurements of aerosol microphysical, optical, and chemical properties were carried out following the wind flow down the AC on board the National Science Foundation (NSF)/NCAR C-130 aircraft on 4 August 2007 at the beginning of the Pacific Atmospheric Sulfur Experiment (PASE). Aboard the NCAR C-130, sample air was delivered to most of the University of Hawaii aerosol sampling package via a solid diffuser (SD) inlet (McNaughton et al. 2007). The APS received air from the Denver University low-turbulence inlet (LTI; Huebert et al. 2004). The LTI draws away the developing turbulent boundary layer within the inlet, leaving laminar flow in which particle trajectories can be well modeled. It has the effect of enhancing large particle concentrations in a manner that is determined by the particle Stokes number and the ratio of the sample to boundary layer suction flows (Wilson et al. 2004). Figure 3 shows LTI enhancement factors together with losses in the bend taking sample flow from the LTI through the fuselage and estimated losses within the tubing to the APS. The first two are known to within about 20% from flow modeling and field projects (Huebert et al. 2004). In contrast, there is considerable uncertainty in the losses within the airplane. At the APS flow rate of 5 Lpm and tube inner diameter of 1.75 cm, flow is laminar, and gravitational settling dominates large particle losses in the 1.5 horizontal meters between the LTI exit and the APS. These were calculated using Eq. (6.49) from Kulkarni et al. (2011), which is not strictly applicable, because bends in the tubing induce mixing not included in the calculation. In addition, there must be some losses resulting from junctions and transition within the tubing. Altogether, the LTI enhancement is almost canceled by tubing losses out to about 10 μm, yielding best-estimate concentrations at the APS within 5% of ambient. At 10 μm uncertainty is about 25%, assuming 50% uncertainty in the losses within the plane.

Other aerosol instrumentation during PASE was effectively identical to the instrument packages deployed aboard the NSF/NCAR C-130 and the National Aeronautics and Space Administration (NASA) DC-8 by the University of Hawaii team during other recent airborne field campaigns (Clarke et al. 2007; McNaughton et al. 2009; Shinozuka et al. 2009). A three-wavelength integrating nephelometer (model 3563, TSI, Inc.) was operated with an inlet impactor (aerodynamic size cut at 1 μm) to periodically remove the larger aerosol in order to resolve contributions to scattering from particles above and below this size. Two condensation nuclei (CN) counters recorded particle number concentrations at 50° (CNcold) and 360°C (CNhot). This allowed nonvolatile particles remaining after heating to 360°C, such as sea salt, low-volatile organics, and soot, to be distinguished from more volatile species, such as sulfates with a 1-Hz time resolution. Size distributions were determined with radial differential mobility analyzers (RDMA; $0.015 < D_p < 0.2$ μm) and long differential mobility analyzers (LDMA; $0.015 < D_p < 0.5$ μm) and an optical particle counter (OPC; $0.2 < D_p < 3$ μm). Both the OPC and RDMA employed thermal volatility to measure distributions in air sampled at about 50°, 150°, and 360°C. This established the volatile and nonvolatile sea salt and other low-volatile components after heating to 360°C.

All instruments were operated inside the aircraft near ambient pressure, but at cabin temperatures. Size distributions from the OPC and DMAs were measured at low humidity. The DMAs used desiccated sheath air to keep RH below 10% and OPC sample air was mixed with filtered desiccated air to reduce RH to 30%–40%. The changes of particle sizes as RH varies from 10% to 40% are small compared to our other size distribution measurement uncertainties. Drying reduces the impact of water uptake by the aerosol on the measured sizes so that the distributions reflect the aerosol components and not the water component (Howell et al. 2006). To calculate the in situ total aerosol surface area at ambient RH we use a simplified algorithm of aerosol hydroscopic growth described in Howell et al. (2006) and Kapustin et al. (2006). First, the aerosol size distributions are divided into accumulation and coarse modes by finding the minima in volume distributions between 0.4 and 1 μm. The accumulation mode is then split into volatile and refractory fractions by using the accumulation mode

volume lost after heating to 350°C. The coarse mode (ambient aerodynamic $D_p \sim 1$ μm) is assumed to be a pure sea salt and behaves according to Tang et al. (1997). The fine and accumulation modes were assumed to be an internal mixture of refractory, low volatile, and volatile components. Although this is a simplification of the AC aerosol chemistry, it captures the basic features. The resulting approximately factor-of-2 growth of the coarse mode from dry to 80% RH is similar to the growth factor for the RED campaign in the same region (Crahan et al. 2004).

In addition to aerosol measurements, a suite of instruments was used aboard the C-130 to conduct precise, high-frequency measurements of various trace gases, as well as liquid water, temperature, pressure, wind velocity, and in situ aerosol parameters. Measurements of DMS, H_2O, and O_3, commonly used for eddy flux correlations (Faloona et al. 2005), are presented here to investigate in-channel MBL evolution and its effect on atmospheric aerosol. Keeping in mind the tendency of the in situ Forward Scattering Spectrometer Probe FSSP-300 to oversize a size distribution, particularly above 8-μm diameter (Reid and Peters 2007; Reid et al. 2006), in this paper we are using APS as the main instrument for sizing coarse particles.

3. Aerosol observations in the Hawaiian natural wind tunnels

Tugboat routes across the Alenuihaha Channel followed four branches (Fig. 1, black) each with a distinct wind speed pattern. Observations from 54 tug boat transects indicate that boundary layer rolls are a very common feature in the MBL near the Hawaiian Islands. Rolls are particularly prevalent in the Alenuihaha Channel and were detected at wind speeds ranging from 7 to 17 m s^{-1} either with or without visible ''cloud streets.'' Figures 2a,b show ceilometer data (30-m vertical resolution) below 1200 m and a MODIS image showing clouds aligned in ''streets'' reflecting boundary layer rolls. The mean trade wind speed upwind of the channel on this date was 11.9 m s^{-1} and the red line indicates the tug boat route. Clouds are evident as high backscatter values in the ceilometer data (Fig. 2a). Note the columns of high backscatter (red) below clouds, and the columns of lower backscatter (blue) in the adjacent cloud-free regions. In situ measurements of dry aerosol scattering and supermicrometer sea salt distribution indicate that near-surface values of aerosol scattering are higher in the updraft regions compared to the downdrafts. Meteorological measurements confirm that the updraft regions below cloud also have higher RH than downdraft region. Because aerosol extinction and backscatter are functions of aerosol concentration and strongly depend on RH, the in situ observations explain the ceilometer's measurements at altitude and suggest that lower backscatter values in the downdrafts are the result of entrainment of FT air that is typically drier and has lower concentrations of aerosol. Figures 2c,d show similar data, but for relatively cloud-free conditions with average wind speeds of 9.7 m s^{-1}. Although the intensity of the backscatter signal is lower, under cloud-free conditions organized structures are still present over similar spatial scales and with higher (lower) ambient aerosol backscattering values in the updraft (downdraft) regions. Lidar observations alone cannot distinguish between organized roll structures and the individual convective elements. Therefore, to support roll structure interpretation we also use the presence of cloud streets on satellite images and sharp oscillations of surface wind speed, RH, and aerosol scattering corresponding to a scale of approximately 1.5–2.5 km.

a. Roll structures

Enhanced aerosol production was commonly measured not only in Alenuihaha but also in the other Hawaiian channels, for example, between Oahu and Molokai (Fig. 4a, region I), or between Molokai and Lanai (same figure, region II). Backscatter measured by the ceilometer (Fig. 4b) is enhanced in the channels but separated by a low backscatter region in the lee of the island of Molokai. This feature is also present in the MODIS image (Fig. 4a) where enhanced surface roughness resulting from higher wind speeds is evident as a darker ocean surface. The darkest region occurs at the narrow eastern gap between Molokai and Maui. This region of elevated surface roughness continues downwind and extends along the north coast of Lanai until it intersects the tugboat transect. Figure 4c is a time series of measurements during the transect and shows the high degree of covariance between meteorological and aerosol parameters. As in the Alenuihaha Channel, relative humidity in the downdrafts is suppressed, apparently resulting from the entrainment of low-RH air from the FT, and enhanced in updrafts that originate at the air–sea interface. Regions with elevated dry scattering (purple) and CN concentration, measured at 300°C (CNhot, red) occur at higher wind speeds, are coincident with moist updrafts, and most likely occur as a result of enhanced sea salt aerosol production from breaking waves (Clarke et al. 2006). As expected, variations in scattering (green) and ceilometer backscatter intensity (dashed blue) at ambient RH are larger than for dry scattering. Region I is clearly dominated by roll-like structures, with weak clouds streets and periodic oscillations of scattering and humidity present (see time

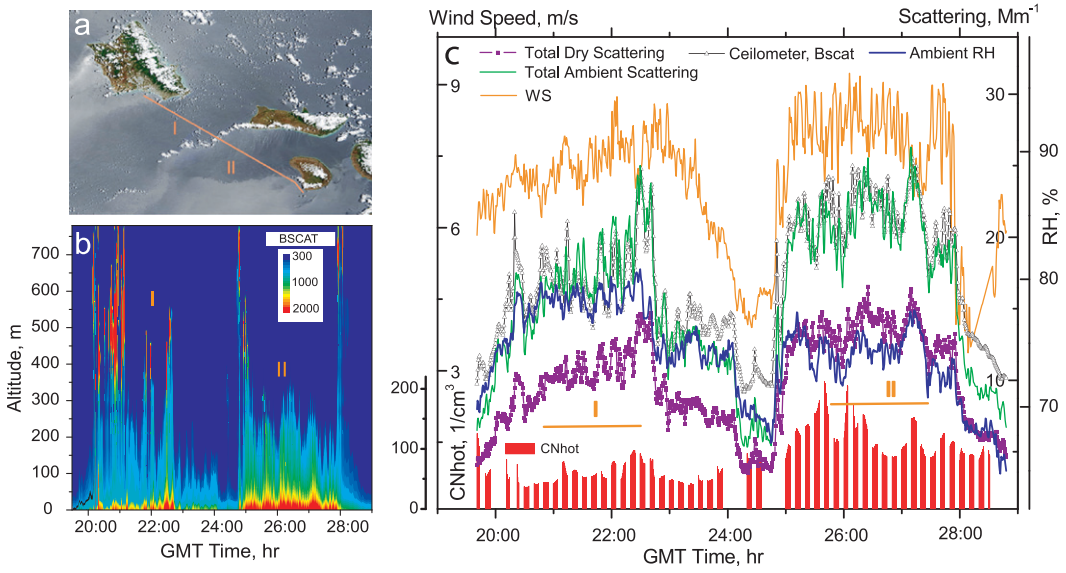

FIG. 4. (a) Tugboat route (orange) superimposed upon MODIS image revealing the related cloud streets structure for region I. (b) Backscatter (10^{-9} m^{-1} $srad^{-1}$) for indicated regions I and II. (c) Time series for the transect that include wind speed (orange), ceilometer backscatter (gray), and nephelometers scattering at 30% RH (magenta) and at ambient RH (green). Also shown is CN measured at 300°C (red).

near 22 h), whereas the presence of rolls in region II is less evident.

Figures 5a,b compare scattering (Fig. 5a) and relative humidity (Fig. 5b) to wind speed for regions I (red) and II (blue) downwind of Molokai. Although region II has higher wind speeds and higher dry scattering values, it has lower relative humidity than region I. Dry scattering, indicative of sea salt aerosol production, is highest in region II where higher wind speeds are maintained over a long fetch (Fig. 4a). For both regions, relative humidity and wind speed appear anticorrelated (Fig. 5b), possibly resulting from entrainment of a dry FT air. Entraining more dry FT air would tend to dilute SSA concentrations and suppress aerosol extinction because of lower ambient RH. Hence, although an overall dependence between SSA and wind speed is evident for all transects (exponential fit in Fig. 5a, magenta), within each region this trend is much less evident (black lines). For the case presented here, the assumption that sea salt concentration depends only on local wind speed, or wind speed history along the fetch, needs to be reexamined. At the scales resolved in this analysis, there appears to be strong coupling between wind speed, sea salt production, and entrainment of FT air, as inferred from RH. This complexity may explain why investigations that examine the production of SSA as a function of wind speed (or other parameters) can display a great deal of variance, even when careful analysis is used to compare nearly identical measurement techniques.

Under typical trade wind conditions, the marine aerosol along the AC shows little continental influence. Aerosol mass, scattering extinction, and backscatter are usually dominated by SSA produced from breaking waves (BWs) in the open ocean and the accelerated channel flow. Figure 5c shows measured supermicron dry (below 40% RH) aerosol light scattering (ambient aerodynamic $D_p > 1$ μm) as a function of wind speed for the AC (open circles). The plot also includes an exponential fit of the scattering data (red symbols) FittedScattering = $(1.9 \pm 0.2) \times \exp[(0.157 \pm 0.05) \times$ WS]. As expected, simple correlation of particle number concentration, mass, or scattering to wind speed alone is rather low (Hoppel et al. 2002). The regression coefficient (R^2) between wind speed and supermicron scattering at 0.55 μm is about 0.54, so only half of the variance in the dry aerosol scattering can be explained by wind speed alone. The high degree of variability of aerosol mass or scattering dependency on wind speed suggests that other processes such as rolls, fetch, variable height of SML, and non-steady-state conditions in the channels are influencing the maintenance of SSA concentration.

b. *Variable fetch and non-steady-state conditions*

Figures 6 and 7 illustrate in situ data collected during C-130 vertical profiles and transect at an altitude of 220 m along the axis of the Alenuihaha Channel on 7 August 2007. The C-130 channel flight track (magenta

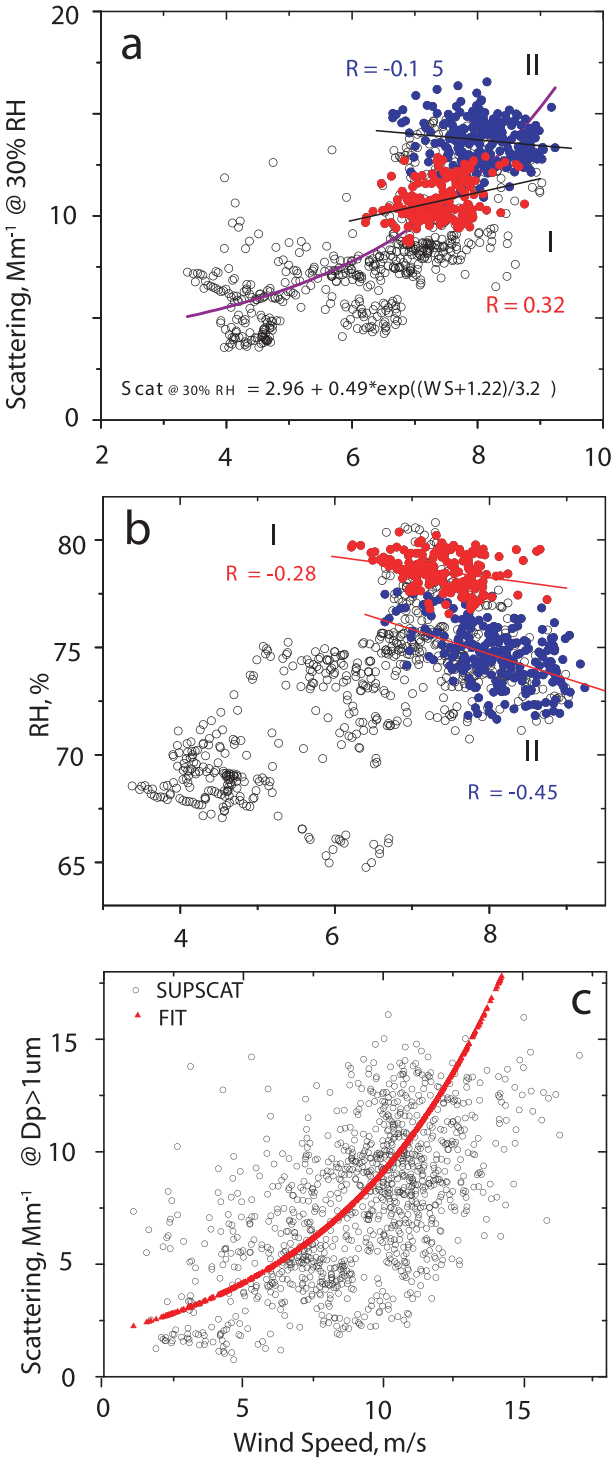

FIG. 5. The relationship of (a) dry scattering and (b) RH from wind speed for regions I (red) and II (blue) in Fig. 4. Open circles correspond to all transect data. (c) Dry supermicron aerosol light scattering (measured during tugboat crossings of the Alenuihaha Channel) vs wind speed. The measured light scattering (open black circles) and an exponential fit of a supermicron scattering (red curve) are shown.

line on Fig. 6a) is divided by flight segments. Also shown are the position of the hydraulic jumps (Smith and Grubisic 1993) and the areas with different sun-glint intensity—the central channel region with enhanced wind and rougher ocean surface, and smoother surface behind the island. Hybrid Single-Particle Lagrangian Integrated Trajectory (HYSPLIT) back trajectories (Draxler and Hess 1998), initiated every 5 s at the C-130 position and colored by measured O_3 concentration, are also shown (Fig. 6a). Trajectories show the gradual increase in O_3 concentration and strong surface wind direction change as air enters the channel. The 15-day back trajectories starting at 300 (red), 1500 (blue) and 2500 (green) m from three locations—above points C and F (Fig. 6a) and near Oahu at the initial ascent position of the C-130—are shown on Fig. 6b. Surface and buffer layer trajectories (red and blue) are similar for all three positions and are typical for MBL trade wind conditions overlaid by synoptic-scale subsidence. Lower FT trajectories are similar for initial ascend position and upwind position F, but are indicative of a significant change of airmass origin for the 2500-m "C" trajectory (green). The C-130's vertical profiles (Fig. 6c) confirm low O_3 values (16 ppbv) throughout the MBL and lower FT for initial ascending profile and highlight the presence of higher O_3 concentrations aloft above the channel (27 ppbv at 2 km). The layer at 2500 m is also characterized by low CO (55 ppbv) and RH (25%).

The ascent profile near Oahu shows a shallow, moist SML that extends up to 500 m. The lower part of the descent profile (below 1 km, part B on Fig. 6a) is not included because it was in the lee of and altered by the Hawaii Island. The depth of MBL for both profiles was near 1700 m.

As the C-130 flew along the channel (Fig. 7), local wind speed increased from ~8 m s^{-1} at 155.8°W to a peak value of 15 m s^{-1} at ~60 km from the channel entrance (blue line on Fig. 7a). All of the distances are taken from channel position at 20.6°N, 155.9°W (location C on Fig. 6a). Also shown on Fig. 7a is the nephelometer light scattering (red). As indicated, the nephelometer periodically switches between total and submicron aerosol scattering. Potential temperature (Θ, red), ozone (black), WD (magenta), APS (D_p > 1 μm) aerosol number concentration (blue), and total aerosol number concentration (UCN, green) along the channel are shown on Fig. 7b. Particle concentrations and total dry scattering increase, while submicrometer scattering (lower branch) remains relatively constant. APS measurements of supermicrometer particle volume size distribution $dV/d\log D_p$ (Fig. 7c) show increasing concentration and a broadening of the distributions. This confirms that the increase in total light

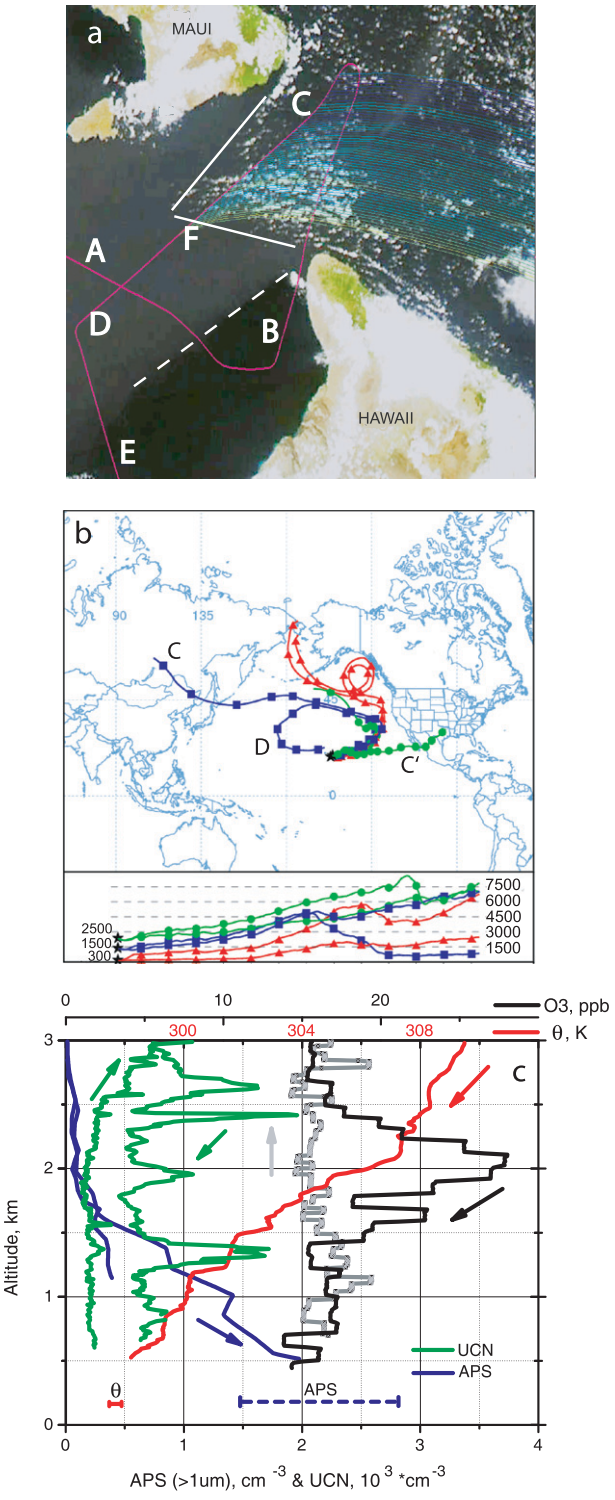

FIG. 6. (a) C-130 channel flight track (magenta) with the following segments: A–B is the descent from 3500 to 220 m, B–C and C–D are the horizontal runs at 220 m, D–E are the beginning of ascent from 220 to 6000 m, and C–F are positions of upwind back trajectories. The hydraulic jump positions (solid white lines), and areas with different sun-glint intensity, with rougher ocean surface within the channel and smoother surface behind the island (separated by dashed white line) are shown. Also shown are HYSPLIT back trajectories (starting every 5 s at C-130 position) colored by measured ozone (O_3) concentration from 16 ppb (blue) to ~17.7 ppb (yellow); (b) 15-day HYSPLIT back trajectories start at 300, 2000, and 2500 m from three locations: C and F on Fig. 7a and near Oahu at the initial ascent position of the C-130; (c) vertical profiles of O_3 (gray: ascent and black: descent), potential temperature (Θ, red), UCN number concentration (green both for ascent and descent), and APS ($d > 1.0\ \mu m$) number concentration (blue) for C-130 initial ascend near Oahu and descent into the channel (segment A–B). Dashed bars at the bottom of (c) indicate range of variability of Θ (red) and APS number concentration (blue) for horizontal run C-D.

scattering is the result of enhanced production of supermicrometer sea salt at higher wind speeds. Also note that increasing particle concentrations and dry scattering are coincident with increasing Θ and rising concentrations of ozone (Fig. 7b). There are very few local anthropogenic sources and no oceanic sources of O_3. Higher O_3 concentration (27 ppbv) at 2 km (Fig. 6c) is likely the only source of the enhanced MBL ozone concentrations and support the conclusion that the rolls and higher wind speeds in the channel enhance turbulent mixing and entrainment of dry FT air into the MBL.

As was mentioned in section 1, a weak hydraulic jump can found in the channel-accelerated flow. The jump manifests itself as a horizontal wind speed decrease at the location ~60 km from the channel entrance (see local minimum on blue line, Fig. 7a). The position of this minimum coincides with the abrupt end of the cloud street pattern (white lines on Fig. 6a).

c. *Whitecaps and sea salt production*

To estimate whitecap coverage along the flight track, we analyze digital images from a forward-looking video camera (one frame per second) using a thresholding technique (Stramska and Petelski 2003). The same middle part of each color image of ocean surface was converted to the black and white (B&W) image using a variable threshold based on a comparison of B&W and original color images. The resulting whitecap ratio W (the ratio of white to the total number of pixels in an image) is shown on Fig. 7d as a function of distance along the channel.

The 10-m wind speed (U_{10}) was estimated from the wind speed measured at the aircraft altitudes under an assumption of logarithmic wind increase with height (Fairall et al. 2003). Compared to average wind speed measured over 220 m, the scaled 10-m wind speed is smaller by ~25%–30%. Measured whitecap fraction W as a function of U_{10} is shown on Fig. 8a (large red dots).

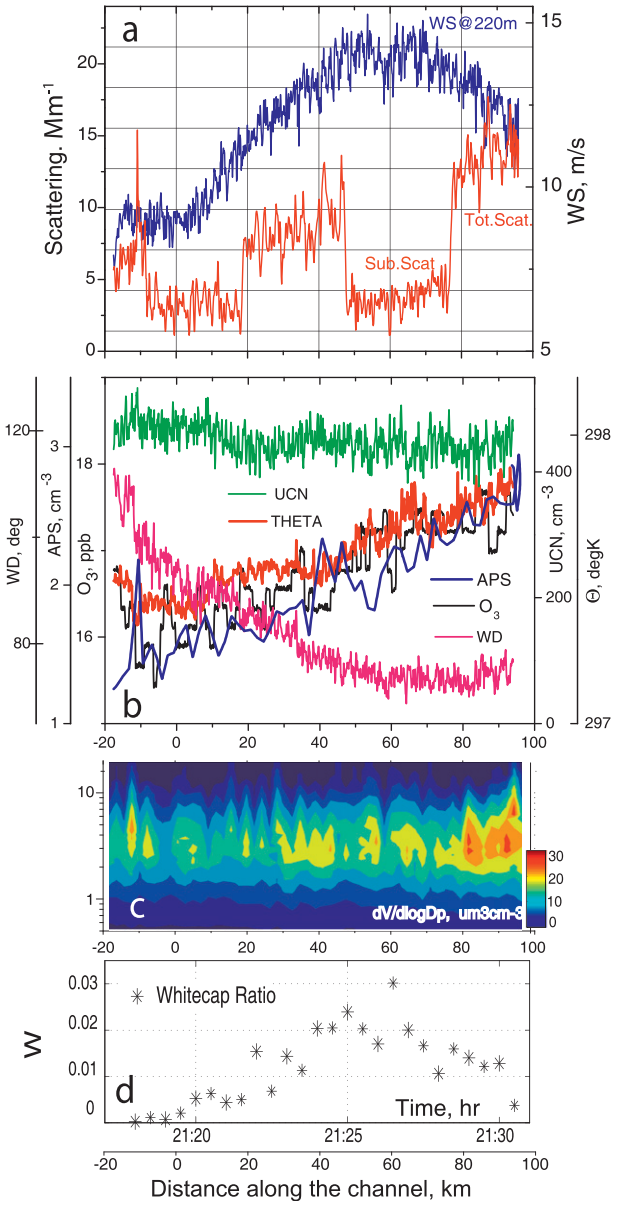

FIG. 7. (a) Wind speed at 220 m (blue) and nephelometer light scattering (red) along the flight track. All of the distances are taken from channel position 20.6°N, 155.9°W (C on a flight track, Fig. 6a). Nephelometer switched between total and submicron aerosol scattering, as indicated. (b) Potential temperature (Θ, red), O_3 (black), WD (magenta), UCN number concentration (green), and APS aerosol number concentration at 1.0 μm $< D_p <$ 10 μm (blue) along the channel. (c) APS volume size distributions $dV/d\log D_p$. (d) Whitecap fraction W along the channel.

Also shown are the Monahan and Muircheartaigh (1980) parameterization (MOM80, black line) and the results of previous (before 2004, black dots) and recent (black rectangular) measurements of W as a function of U_{10} (all from de Leeuw et al. 2011). The measured W for the Alenuihaha Channel data is well within the range of variability of published data. The dependence of SSA concentration and W is a function of U_{10} measured in the channel shown on Fig. 8b. Red dots represent the measured APS number concentration (1 μm $< D_p <$ 10 μm, N_{aps}), the blue line and symbols correspond to the 30-s bin average of N_{aps}. Measured W is shown as a black line and symbols. Arrows indicate the direction of flight along the segment from C to D (Fig. 6a). Channel whitecap coverage increases from 0% to 2.5% with U_{10} (from 7.2 to 11 m s^{-1}) and decreases to ~1% when wind speed drops to 9.5 m s^{-1} (Fig. 8b, black). Corresponding integral number concentration N_{aps} (APS dry geometric diameters 1.0 $< D_p <$ 10 μm) continues to increase even after U_{10} and W start to decrease. The resulting essentially nonlinear dependency of N_{aps} (Fig. 8b, red dots) from U_{10} shows that airmass history and fetch are as important as wind speed in determining sea salt aerosol concentrations. At the same time W does not show Callaghan et al.'s (2008) observed hysteresis dependency on wind speed history, probably because U_{10} was below 11 m s^{-1}.

4. Production flux estimations

As mentioned earlier, the CBM based on aircraft measurements of SSA buildup during offshore advection has been implemented only once by Reid et al. (2001). Among the reasons why there were no other attempts to apply CBM are the infrequent appearance of necessary weather conditions (proper wind direction and wind speed range), a high level of background aerosol concentration ($dN/d\log D_p > 1000$ cm^{-3} for $D_p =$ 0.2 μm) interfering with the ability to measure changes resulting from sea salt, and some concerns that a fully developed sea state is essentially impossible to obtain in the nearshore region.

In comparison, the Alenuihaha Channel has a broad and uniform open-ocean upstream area with a low steady-state background aerosol concentration, usually below 350 cm^{-3}. The channel provides predictable enhanced wind flow aligned along the 100-km fetch that generates enhanced whitecaps and SSA. This combination of the unique AC features represents a challenging but interesting environment for production flux estimates using a modified version of CBM. While the relatively clean air and well-defined fetch are assets, the AC suffers from a couple of problems that require modification of the basic CBM algorithm: the wind speed is not constant and the mixed layer depth can change dynamically and as the buffer layer air mixes in.

In the assumption of stationary but non-steady-state conditions with constant wind the SSA concentration buildup in the advected air column (a box advection model with no entrainment) is equal to the upward

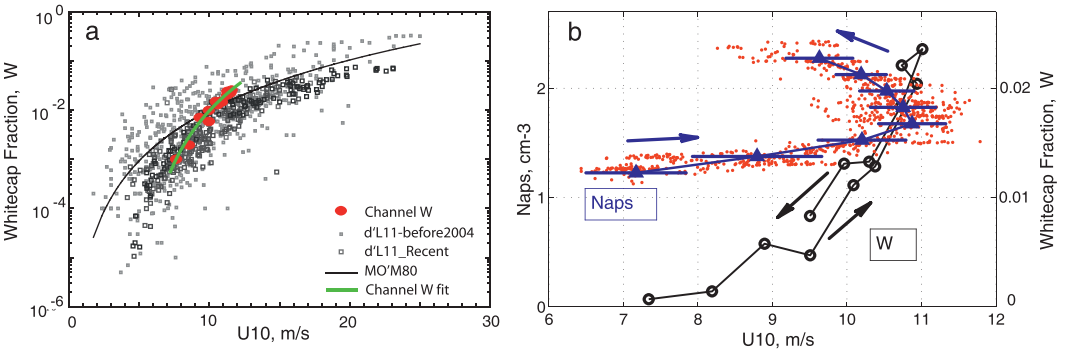

FIG. 8. (a) Whitecap fraction W as a function of wind speed at 10 m above the sea surface. C-130 channel flight data (red solid dots), $U^{3.70}$ fit of measured channel W data (green line), Monahan and Muircheartaigh, 1980 parameterization (black line), and results of previous and recent W vs U_{10} measurements (all from de Leeuw et al. 2011; black dots and rectangles). (b) C-130 channel flight SSA and whitecaps evolution. Measured APS number concentration (red dots) with 30-s bin average results (blue). Measured W is shown (black line and symbols), with the direction of the flight from C to D indicated (arrows, Fig. 6a).

production SSA flux minus the downward flux from dry deposition and sedimentation (Reid et al. 2001). For a size of particles below 10 μm, the deposition term is small, so effective SSA production flux is

$$F_{\text{eff}} = d\text{Ccol}/dt \sim U_{10} \times (d\text{Ccol}/dx), \qquad (1)$$

where Ccol is an aerosol column burden and t is time. This method requires sufficiently frequent measurements of the $dN/d\log D_p$ and Ccol that the derivative of Ccol with respect to x can be calculated (Lewis and Schwartz 2004). By replacing derivatives with differences and further assuming that all particles are nearly uniformly and rapidly mixed over the MBL, F_{eff} can be obtained.

Unlike the wind conditions of Reid et al. (2001), surface wind for the channel area is not constant. Therefore, the time derivative was taken in a column moving with the wind speed in a Lagrangian frame of reference. Positions along the channel of the Lagrangian air column are shown in Fig. 9a. The black line represents wind speed U_{10}, and the red dashed lines indicate the column positions at five consecutive advection steps, so that the width of each is proportional to the mean wind speed (red diamonds on Fig. 9a) for each interval. Because LDMA or DMA size distributions were measured approximately each 10 km, OPC was at 300°C, and APS distribution was taken every 200 m, the advection steps were wide enough to ensure at least one combined size distribution per step. For an expected vertical velocities of about 1 m s^{-1} (if rolls are present), 500 m of SML will be mixed in an about 10 min. Because each of the intervals is about 15–20 km apart the differences in concentration reflect about 25–30 min of buildup, such that the rapid mixing assumption is reasonable.

Figure 9b shows the combined LDMA, OPC at 300°C, and APS number size distributions $dN/d\log D_p$ at 80% RH for steps 3 (black) and 5 (red line). A clearly visible wind-dependent increase of particles both in coarse (wet diameter $D_p > 0.8$ μm) and accumulation modes ($D_p > 0.1$ μm) is evident. The change in Aitken mode ($D_p < 0.1$ μm) is less clear. Unlike the larger OPC sizes, these sizes are not thermally resolved and are in size ranges likely to be entrained from the clean FT (Clarke et al. 2006). Because these were not characterized by appropriate profiles for this flight of opportunity, it is not possible to assess variability over this size range.

To calculate aerosol column burden we also need to know the SML height along the channel. During this part of flight the C-130 made two vertical profile measurements: one near Oahu and one at the bottom of the channel well behind the hydraulic jump line location (see Fig. 6a). For both profiles the height of MBL was near 1700 m. The SML for ascent near Oahu has a depth ~500 m. As discussed before a substantial decrease in TWI height can exist upwind of hydraulic jump lines, but changes in SML height are not obvious. Dashed bars at the bottom of Fig. 6c indicate a range of variability of Θ (red) and an APS number concentration (blue) for the horizontal run C–D; Θ is increasing by 0.3 K from 297.5 to 297.8 K (Fig. 7c). Keeping in mind that the average Θ of the overlying buffer layer (~500–1100 m) is ~299 K and SML height (Hsml) is about 500 m, possible dilution of the SML column resulting from entrainment during 80 km of the AC run must be 20% or less. Similar 10%–20% replenishment of the SML air from the overlying buffer layer can be obtained assuming a typical developed SML roll structure entrainment rate of 1.0–1.5 cm s^{-1} (Conley et al. 2011; Conley et al. 2009), wind speed 10 of m s^{-1}, 80 km of the AC run, and Hsml = 400–800 m.

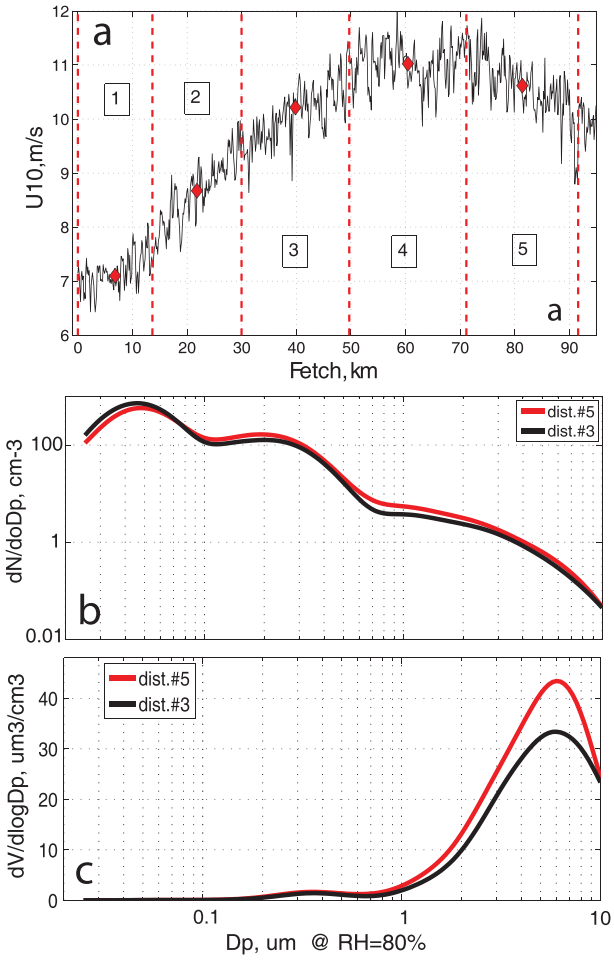

FIG. 9. (a) Position along the channel of moving with U_{10} wind speed Lagrangian air column. U_{10} (black line), column position in five equally spaced time intervals (red dashed lines), and mean U_{10} wind (red diamonds) are shown. Mean combined (b) number and (c) volume size distributions at column positions 3 (black) and 5 (red) and 220-m altitude.

Because of the relatively small wind speed changes at the area of maximum U_{10} (positions 3, 4, and 5 on Fig. 9a) we can estimate SSSF using the CBM approach of Reid et al. 2001 with constant wind speed conditions. For example, the change in the column burden between positions 3 and 4 is simply $\Delta_{43} = [(dN/d\log D_p)_4 - (dN/d\log D_p)_3] \times 10^6\ \mathrm{m}^{-3}$, the SML height is Hsml = 500 m, the average wind speed is $[U_{10}]_{34} = 10.7\ \mathrm{m\ s}^{-1}$, the fetch is $dx = 2 \times 10^4$ m, and the effective sea spray flux is

$$F_{\mathrm{eff}} = [U_{10}]_{34} \times [\Delta(dN/d\log D_p)_{43}/dx] \times \mathrm{Hsml} = \Delta(dN/d\log D_p)_{43} \times 2.67 \times 10^5\ \mathrm{m}^{-2}\,\mathrm{s}^{-1}. \quad (2)$$

Combining flux values derived for positions (3, 4), (4, 5), and (3, 5) together allows for the estimation of the mean effective SSA production flux at wind speed $U_{10} \sim 10.7\ \mathrm{m\ s}^{-1}$ (Fig. 10, heavy red line and symbols). A combined uncertainty in F_{eff} (red dashed lines) of about 100% was estimated from the standard deviation of the size distribution differences, C-130 sampling efficiency for large sea salt particles, uncertainties in SML height, U_{10} wind speed, and estimates of the replenishment rate.

Using a simplifying assumption that the dependences on particle size and environmental variables (wind speed) can be separated (de Leeuw et al. 2011) and based on reasonably good fit of our measured W by $W \sim U_{10}^{3.70}$, the derived SSA production flux (2) can be written as

$$F_{\mathrm{eff}} = (U_{10}^{3.70}/10.7^{3.70}) \times \Delta(dN/d\log D_p)_{43} \times 2.67 \times 10^5\ \mathrm{m}^{-2}\,\mathrm{s}^{-1}. \quad (3)$$

After fitting derived flux with a sum of two lognormal distributions, the parameterized SSSF can be written as

$$F_{\mathrm{eff}} = U_{10}^{3.70} \times \sum_{i=1}^{2} \frac{N_i}{\sqrt{2\pi}\log\sigma_i} \exp\left[-\frac{1}{2}\left(\frac{\log D_p - \log D_i}{\log\sigma_i}\right)^2\right], \quad (4)$$

where N_i are amplitudes, D_i are median diameters, σ_i are geometric standard deviations, and $0.15\ \mu\mathrm{m} < D_p < 10\ \mu\mathrm{m}$.

Also shown in Fig. 10 are the lognormal fit (4) of the derived flux (blue dashed line), and source functions from Lewis and Schwartz (2004, dark cyan line) and Clarke et al. (2006, black lines) both for wind speed $U_{10} = 12\ \mathrm{m\ s}^{-1}$ (heavy lines) and $U_{10} = 8\ \mathrm{m\ s}^{-1}$ (thin lines). Parameters of a bimodal lognormal SSA flux fit N_i, D_i, and σ_i are presented in Table 1.

Our derived source flux compares reasonably well to the results of Clarke et al. (2006), and in particular over the range $0.3\ \mu\mathrm{m} < D_p < 1.5\ \mu\mathrm{m}$. For particles above 1.5–2 μm our lower value for flux is possibly due to an underestimation of the coarse-mode aerosol compared to ground-based measurements used for Clarke et al. (2006). However, some enhancement of coarse particle concentration is also possible in the earlier study arising from the correction algorithm applied.

5. Conclusions

We use ship- and aircraft-based observations of meteorological parameters and aerosols in Hawaii's orographic natural "wind tunnel" for the study of sea salt aerosol (SSA) production, evolution, and related optical

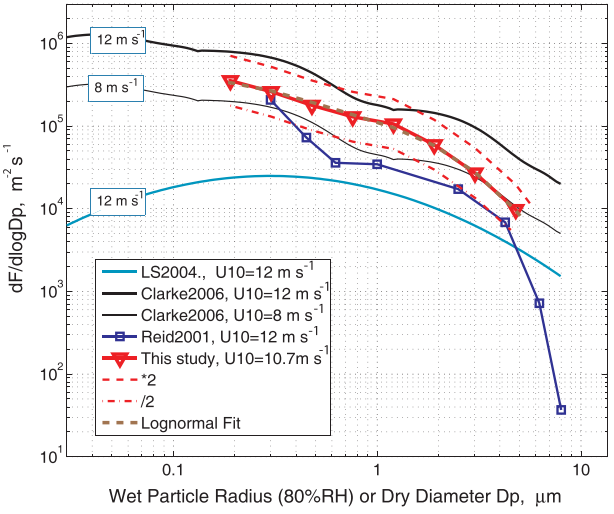

FIG. 10. Derived size-dependent SSA production flux evaluated for wind speed $U_{10} = 10.7$ m s^{-1} (heavy red line and symbols); */2 uncertainty range is shown (dashed red line). Also shown is the lognormal fit of derived flux (brown), source functions of Lewis and Schwartz (2004) at $U_{10} = 12$ m s^{-1} (dark cyan), Clarke et al. (2006) at $U_{10} = 12$ m s^{-1} and $U_{10} = 8$ m s^{-1} (heavy and thin black lines), and Reid et al. (2001) at $U_{10} = 12$ m s^{-1} (blue line and symbols).

effects under clean oceanic conditions. There are certain advantages of channel measurements, such as a broad, clean, and uniform upstream area usually filled with clean background aerosol, stationary flow, topography-induced steady-state accelerated wind flow that can nearly double over trade wind speed with a well-defined 100 km of fetch.

During a flight along the channel, we found many of the features expected in flow through a gap, including airflow accelerated to twice that of the upstream trade winds, a hydraulic jump at the maximum wind speed location, and greatly increased concentrations of sea salt aerosol. Enhanced concentrations relative to upstream conditions were found for particles from 20 nm to 5 μm, though concentrations of particles below 100 nm dropped in the region of the highest airspeed, suggesting that dilution from the buffer layer exceeded sea salt production in that size range. This is consistent with ozone concentrations that rose with distance downstream.

Studies of aerosol in the remote marine atmosphere, in particular in the formation of primary sea salt aerosol by wind and breaking waves, are complicated by mesoscale processes such as synoptic meteorology and boundary layer structure. Measurements in the channel and elsewhere can be complicated due to entrainment associated with presence of organized structures (rolls). We find that marine boundary layer (MBL) rolls are a common occurrence near the Hawaiian Islands even when cloud streets are not visible in satellite imagery.

TABLE 1. Parameters of a bimodal lognormal SSA flux fit; N_i are amplitudes, D_i are median diameters, σ_i are geometric standard deviations, and 0.15 μm $< D_p <$ 8 μm.

Mode	N_i	D_i	σ_i
1	64.3	0.12	2.8
2	8.9	1.00	2.2

The presence of rolls tends to enhance the variability of ambient aerosol concentration, extinction, probably affects production of primary sea salt aerosol and entrainment of dry, relatively particle-free air from above.

We demonstrate that organized boundary layer structures (rolls) are a common feature of the Hawaiian channels, which has influence on the boundary layer aerosol properties. When entrained into roll updrafts these aerosol enhance ambient light scattering. In the downdrafts, ambient relative humidity is lower and particle numbers appear diluted through more vigorous entrainment of air from the FT, which is typically drier. We explore the possibility of channel measurements of the size-dependent flux of SSA using a concentration buildup method at a surface wind speed range from 7 to 11 m s^{-1}. A simple budget technique in the region with maximum winds gave fluxes of SSA that are similar to earlier studies (Clarke et al. 2006). The production of SSA particles with a dry diameter as small as 0.18 μm was observed. More sophisticated modeling with inversion techniques could be applied to the entire channel but need to be accompanied by more complete aircraft profiles and measurements of mixed layer height (e.g., lidar) and entrainment from the buffer layer than was afforded by this flight of opportunity.

Acknowledgments. This work was made possible by the grants from Office of Naval Research (ONR Grant N000014-07-0031) and National Science Foundation (NSF Grant ATM-0627227). The authors thank the crews of the Young Brothers, Ltd., tugboat and NCAR C-130 for their assistance in collecting this data.

REFERENCES

Atkinson, B. W., and J. W. Zhang, 1996: Mesoscale shallow convection in the atmosphere. *Rev. Geophys.,* **34,** 403–431.

Bigg, E. K., C. Leck, and E. D. Nilsson, 1996: Sudden changes in arctic atmospheric aerosol concentrations during summer and autumn. *Tellus,* **48B,** 254–271.

——, ——, and ——, 2001: Sudden changes in aerosol and gas concentrations in the central Arctic marine boundary layer: Causes and consequences. *J. Geophys. Res.,* **106** (D23), 32 167–32 185.

Brooks, I. M., and D. P. Rogers, 1997: Aircraft observations of boundary layer rolls off the coast of California. *J. Atmos. Sci.,* **54,** 1834–1849.

Brummer, B., 1999: Roll and cell convection in wintertime arctic cold-air outbreaks. *J. Atmos. Sci.,* **56,** 2613–2636.

——, S. Bakan, and H. Hinzpeter, 1985: Kontur: Observations of cloud streets and open cellular structures. *Dyn. Atmos. Oceans,* **9,** 281–296.

Callaghan, A., G. de Leeuw, L. Cohen, and C. D. O'Dowd, 2008: Relationship of oceanic whitecap coverage to wind speed and wind history. *Geophys. Res. Lett.,* **35,** L23609, doi:10.1029/2008GL036165.

Clarke, A. D., and V. N. Kapustin, 2002: A Pacific Aerosol Survey. Part I: A decade of data on production, transport, evolution and mixing in the troposphere. *J. Atmos. Sci.,* **59,** 363–382.

——, and ——, 2003: The Shoreline Environment Aerosol Study (SEAS): A context for marine aerosol measurements influenced by a coastal environment and long-range transport. *J. Atmos. Oceanic Technol.,* **20,** 1351–1361.

——, J. L. Varner, F. Eisele, R. L. Mauldin, D. Tanner, and M. Litchy, 1998a: Particle production in the remote marine atmosphere: Cloud outflow and subsidence during ACE-1. *J. Geophys. Res.,* **103,** 16 397–16 409.

——, and Coauthors, 1998b: Particle nucleation in the tropical boundary layer and its coupling to marine sulfur sources. *Science,* **282,** 89–92.

——, S. Owens, and J. Zhou, 2006: An ultrafine sea-salt flux from breaking waves: Implications for cloud condensation nuclei in the remote marine atmosphere. *J. Geophys. Res.,* **111,** D06202, doi:10.1029/2005JD006565.

——, and Coauthors, 2007: Biomass burning and pollution aerosol over North America: Organic components and their influence on spectral optical properties and humidification response. *J. Geophys. Res.,* **112,** D12S18, doi:10.1029/2006JD007777.

Conley, S. A., I. Faloona, G. H. Miller, D. H. Lenschow, B. Blomquist, and A. Bandy, 2009: Closing the dimethyl sulfide budget in the tropical marine boundary layer during the Pacific Atmospheric Sulfur Experiment. *Atmos. Chem. Phys.,* **9,** 8745–8756.

——, and Coauthors, 2011: A complete dynamical ozone budget measured in the tropical marine boundary layer during PASE. *J. Atmos. Chem.,* **68,** 55–70, doi:10.1007/s10874-011-9195-0.

Crahan, K. K., D. A. Hegg, D. S. Covert, H. Jonsson, J. S. Reid, D. Khelif, and B. J. Brooks, 2004: Speciation of organic aerosols in the tropical mid-Pacific and their relationship to light scattering. *J. Atmos. Sci.,* **61,** 2544–2558.

de Leeuw, G., E. L Andreas, M. D. Anguelova, C. W. Fairall, E. R. Lewis, C. D. O'Dowd, M. Schulz, and S. E. Schwartz, 2011: Production flux of sea spray aerosol. *Rev. Geophys.,* **49,** RG2001, doi:10.1029/2010RG000349.

Dupont, E., J. Pelon, and C. Flamant, 1994: Study of the moist convective boundary-layer structure by backscattering lidar. *Bound.-Layer Meteor.,* **69,** 1–25.

Engelmann, R., U. Wandinger, A. Ansmann, D. Muller, E. Zeromskis, D. Althausen, and B. Wehner, 2008: Lidar observations of the vertical aerosol flux in the planetary boundary layer. *J. Atmos. Oceanic Technol.,* **25,** 1296–1306.

Fairall, C. W., E. F. Bradley, J. E. Hare, A. A. Grachev, and J. B. Edson, 2003: Bulk parameterization of air-sea fluxes: Updates and verification for the COARE algorithm. *J. Climate,* **16,** 571–591.

Faloona, I., D. Lenschow, and T. Campos, 2005: Observations of entrainment of Eastern Pacific marine stratocumulus using three conserved scalars. *J. Atmos. Sci.,* **62,** 3268–3285.

Gabersek, S., and D. R. Durran, 2004: Gap flows through idealized topography. Part I: Forcing by large-scale winds in the nonrotating limit. *J. Atmos. Sci.,* **61,** 2846–2862.

Hoppel, W. A., G. M. Frick, and J. W. Fitzgerald, 2002: Surface source function for sea-salt aerosol and aerosol dry deposition to the ocean surface. *J. Geophys. Res.,* **107,** 4382, doi:10.1029/2001JD002014.

Howell, S. G., A. D. Clarke, Y. Shinozuka, V. N. Kapustin, C. S. McNaughton, B. J. Huebert, S. Doherty, and T. Anderson, 2006: The influence of relative humidity upon pollution and dust during ACE-Asia: Size distributions and implications for optical properties. *J. Geophys. Res.,* **111,** D06205, doi:10.1029/2004JD005759.

Huang, Q., J. H. Marsham, D. J. Parker, W. S. Tian, and T. Weckwerth, 2009: A Comparison of roll and nonroll convection and the subsequent deepening moist convection: An LEM case study based on SCMS data. *Mon. Wea. Rev.,* **137,** 350–365.

Huebert, B. J., and Coauthors, 2004: PELTI: Measuring the passing efficiency of an airborne low turbulence aerosol inlet. *Aerosol Sci. Technol.,* **38,** 803–826, doi:10.1080/027868290500823.

Kalogiros, J., and Q. Wang, 2011: Aircraft observations of sea-surface turbulent fluxes near the California coast. *Bound.-Layer Meteor.,* **139,** 283–306.

Kapustin, V. N., A. D. Clarke, Y. Shinozuka, S. Howell, V. Brekhovskikh, T. Nakajima, and A. Higurashi, 2006: On the determination of a cloud condensation nuclei from satellite: Challenges and possibilities. *J. Geophys. Res.,* **111,** D04202, doi:10.1029/2004JD005527.

Kiemle, C., M. Kastner, and G. Ehret, 1995: The convective boundary-layer structure from lidar and radiosonde measurements during the EFEDA-91 campaign. *J. Atmos. Oceanic Technol.,* **12,** 771–782.

Kulkarni, P., P. A. Baron, and K. Willeke, 2011: *Aerosol Measurement: Principles, Techniques, and Applications*. 3rd ed. John Wiley & Sons, 904 pp.

Kulmala, M., H. Vehkamäki, T. Petäjä, M. Dal Maso, A. Lauri, V.-M. Kerminen, W. Birmili, and P. H. McMurry, 2004: Formation and growth rates of ultrafine atmospheric particles: A review of observations. *J. Aerosol Sci.,* **35,** 143–176.

LeMone, M. A., 1973: The structure and dynamics of horizontal roll vortices in the planetary boundary layer. *J. Atmos. Sci.,* **30,** 1077–1091.

——, 1976: Modulation of turbulence energy by longitudinal rolls in an unstable planetary boundary layer. *J. Atmos. Sci.,* **33,** 1308–1320.

Lewis, E. R., and S. E. Schwartz, 2004: *Sea Salt Aerosol Production: Mechanisms, Methods, Measurements and Models*. *Geophys. Monogr.,* Vol. 152, Amer. Geophys. Union, 413 pp.

Marsham, J. H., D. J. Parker, C. M. Grams, B. T. Johnson, W. M. F. Grey, and A. N. Ross, 2008: Observations of mesoscale and boundary-layer scale circulations affecting dust transport and uplift over the Sahara. *Atmos. Chem. Phys.,* **8,** 6979–6993.

McNaughton, C. S., and Coauthors, 2007: Results from the DC-8 Inlet Characterization Experiment (DICE): Airborne versus surface sampling of mineral dust and sea salt aerosols. *Aerosol Sci. Technol.,* **41,** 136–159.

——, and Coauthors, 2009: Observations of heterogeneous reactions between Asian pollution and mineral dust over the Eastern North Pacific during INTEX-B. *Atmos. Chem. Phys.,* **9,** 8283–8308, doi:10.5194/acp-9-8283-2009.

Melfi, S. H., J. D. Spinhirne, S. H. Chou, and S. P. Palm, 1985: Lidar observations of vertically organized convection in the planetary

boundary-layer over the ocean. *J. Climate Appl. Meteor.,* **24,** 806–821.

Nilsson, E. D., U. Rannik, E. Swietlicki, C. Leck, P. P. Aalto, J. Zhou, and M. Norman, 2001: Turbulent aerosol fluxes over the Arctic Ocean 2. Wind-driven sources from the sea. *J. Geophys. Res.,* **106** (D23), 32 139–32 154.

O'Dowd, C. D., and G. De Leeuw, 2007: Marine aerosol production: A review of the current knowledge. *Philos. Trans. Roy. Soc. London,* **365A,** 1753–1774.

Raes, F., R. Van Dingenen, E. Vignati, J. Wilson, J. P. Putaud, J. H. Seinfeld, and P. Adams, 2000: Formation and cycling of aerosols in the global troposphere. *Atmos. Environ.,* **34,** 4215–4240.

Reid, J. S., and T. M. Peters, 2007: Update to ''Reconciliation of coarse mode sea-salt aerosol particle size measurements and parameterizations at a subtropical ocean receptor site'' regarding the use of aerodynamic particle sizers in marine environments. *J. Geophys. Res.,* **112,** D04202, doi:10.1029/2006JD007501.

——, H. H. Jonsson, M. H. Smith, and A. Smirnov, 2001: Evolution of the vertical profile and flux of large sea-salt particles in a coastal zone. *J. Geophys. Res.,* **106,** 12 039–12 054.

——, and Coauthors, 2006: Reconciliation of coarse mode sea-salt aerosol particle size measurements and parameterizations at a subtropical ocean receptor site. *J. Geophys. Res.,* **111,** D02202, doi:10.1029/2005JD006200.

Shinozuka, Y., A. D. Clarke, S. G. Howell, V. N. Kapustin, and B. J. Huebert, 2004: Sea-salt vertical profiles over the Southern and tropical Pacific oceans: Microphysics, optical properties, spatial variability, and variations with wind speed. *J. Geophys. Res.,* **109,** D24201, doi:10.1029/2004JD004975.

——, and Coauthors, 2009: Aerosol optical properties relevant to regional remote sensing of CCN activity and links to their organic mass fraction: Airborne observations over Central Mexico and the US West Coast during MILAGRO/INTEX-B. *Atmos. Chem. Phys.,* **9,** 6727–6742.

Smith, R. B., and V. Grubisic, 1993: Aerial observations of Hawaii wake. *J. Atmos. Sci.,* **50,** 3728–3750.

Solomon, D. Q. S., M. Manning, Z. Chen, M. Marquis, K. B. Averyt, M. Tignor, and H. L. Miller, Eds., 2007: Technical summary. *Climate Change 2007: The Physical Science Basis*, Cambridge University Press.

Stramska, M., and T. Petelski, 2003: Observations of oceanic whitecaps in the north polar waters of the Atlantic. *J. Geophys. Res.,* **108,** 3086, doi:10.1029/2002JC001321.

Tang, I. N., A. C. Tridico, and K. H. Fung, 1997: Thermodynamic and optical properties of sea salt aerosols. *J. Geophys. Res.,* **102,** 23 269–23 276.

Weckwerth, T. M., J. W. Wilson, R. M. Wakimoto, and N. A. Crook, 1997: Horizontal convective rolls: Determining the environmental conditions supporting their existence and characteristics. *Mon. Wea. Rev.,* **125,** 505–526.

Wilson, J. C., and Coauthors, 2004: Function and performance of a low turbulence inlet for sampling super-micron particles from aircraft platforms. *Aerosol Sci. Technol.,* **38,** 790–802.

Yang, Y., and Y. L. Chen, 2008: Effects of terrain heights and sizes on island-scale circulations and rainfall for the island of Hawaii during HaRP. *Mon. Wea. Rev.,* **136,** 120–146.

——, ——, and F. M. Fujioka, 2008: Effects of trade-wind strength and direction on the leeside circulations and rainfall of the Island of Hawaii. *Mon. Wea. Rev.,* **136,** 4799–4818.

Young, G. S., D. A. R. Kristovich, M. R. Hjelmfelt, and R. C. Foster, 2002: Rolls, streets, waves, and more—A review of quasi-two-dimensional structures in the atmospheric boundary layer. *Bull. Amer. Meteor. Soc.,* **83,** 997–1001.

Zangl, G., 2002: Stratified flow over a mountain with a gap: Linear theory and numerical simulations. *Quart. J. Roy. Meteor. Soc.,* **128,** 927–949.